applied sciences

MDPI

Article

Carbon Dioxide Adsorption on Carbon Nanofibers with Different Porous Structures

Yu-Chun Chiang [1,2,*], Chih-Cheng Huang [1] and Wei-Ting Chin [1]

[1] Department of Mechanical Engineering, Yuan Ze University, Taoyuan 320, Taiwan; s1060807@mail.yzu.edu.tw (C.-C.H.); s1060806@mail.yzu.edu.tw (W.-T.C.)
[2] Fuel Cell Center, Yuan Ze University, Taoyuan 320, Taiwan
* Correspondence: ycchiang@saturn.yzu.edu.tw; Tel.: +886-3463-8800 (ext. 2476)

Abstract: Electrospinning techniques have become an efficient way to produce continuous and porous carbon nanofibers. In view of CO_2 capture as one of the important works for alleviating global warming, this study intended to synthesize polyacrylonitrile (PAN)-based activated carbon nanofibers (ACNFs) using electrospinning processes for CO_2 capture. Different structures of PAN-based ACNFs were prepared, including solid, hollow, and porous nanofibers, where poly(methyl methacrylate) (PMMA) was selected as the sacrificing core or pore generator. The results showed that the PMMA could be removed successfully at a carbonization temperature of 900 °C, forming the hollow or porous ACNFs. The diameters of the ACNFs ranged from 500 to 900 nm, and the shell thickness of the hollow ACNFs was approximately 70–110 nm. The solid ACNFs and hollow ACNFs were microporous materials, while the porous ACNFs were characterized by hierarchical pore structures. The hollow ACNFs and porous ACNFs possessed higher specific surface areas than that of the solid ACNFs, while the solid ACNFs exhibited the highest microporosity (94%). The CO_2 adsorption capacity on the ACNFs was highly dependent on the ratio of $V_{<0.7\ nm}$ to V_t, the ratio of V_{mi} to V_t, and the N-containing functional groups. The CO_2 adsorption breakthrough curves could be curve-fitted well with the Yoon and Nelson model. Furthermore, the 10 cyclic tests demonstrated that the ACNFs are promising adsorbents.

Keywords: activated carbon nanofibers; electrospinning; carbon dioxide; adsorption breakthrough

Citation: Chiang, Y.-C.; Huang, C.-C.; Chin, W.-T. Carbon Dioxide Adsorption on Carbon Nanofibers with Different Porous Structures. *Appl. Sci.* **2021**, *11*, 7724. https://doi.org/10.3390/app11167724

Academic Editors: Wen-Hsiang Hsieh, Jia-Shing Sheu and Minvydas Ragulskis

Received: 31 July 2021
Accepted: 20 August 2021
Published: 22 August 2021

1. Introduction

Carbon fibers are of great significance in scientific and technological applications because of their high specific surface areas, high surface area to volume ratios, easy functionalization, superior mechanical properties, outstanding flexibility, etc., particularly when the carbon fibers are reduced to nanoscale. These superior properties make the carbon nanofibers show excellent performances in several applications (e.g., gas adsorption, gas storage, filter media, sensors, drug delivery, tissue engineering, protective clothing, etc.) [1–3]. Drawing [4,5], template synthesis [6,7], phase separation [8], self-assembly [9,10], and electrospinning [11,12] have all been investigated to produce nanofibers successfully. Compared with other methods, electrospinning is acknowledged as a simple, inexpensive, and efficient process to draw out polymers into continuous fibers with diameters ranging from submicrons to nanometers [3,13].

Despite this, the electrospinning process is very intricate, and can be described as the interactions of several physical instability processes [13,14], such as applied electrical voltage, tip-to-collector distance, and injection rate. The concentration and viscosity of the polymer solution have the most significant influence on the electrospinning process and the resultant fiber morphology [3]. In effect, the diameter of the electrospun nanofibers is influenced not only by the concentration of the polymer and the solution viscosity, but also by its molecular conformation [14,15]. In the dilute concentration range, the electrospinning of polymer solutions only forms polymer droplets, due to an insufficient chain overlap. As

the concentration is increased, beaded fibers and further uniform fibers can be observed sequentially [16]. A fibrous structure is stabilized above a minimum concentration, but the fiber diameter increases with molecular weight and concentration [15]. For the polymers with higher molecular weights, uniform fibers can be formed at a lower polymer concentration compared with those having lower molecular weights [17]. Thus, the intermolecular entanglements play an important role in stabilizing the fibrous structure [18].

The co-electrospinning of polymer solutions from a spinneret set containing two coaxial capillaries has been developed to serve as an alternative technique for the fabrication of hollow fibers [19]. Using this method, co-electrospinning immiscible and miscible pairs of polymer solutions forms nanofibers with core/shell structures [19]. Subsequently, the core material can be removed by thermal decomposition [19,20] or extraction with mineral oil or solvent [21]. In general, it is suggested that the core-polymer capillary protrude ~1 mm below the end of the shell capillary to produce a good Taylor cone at the end of the nozzle [19,22]. Kaerkitcha et al. [22] found that good morphologies of polyacrylonitrile (PAN)/poly(methyl methacrylate) (PMMA) nanofibers were obtained from the coaxial nozzle electrospinning at 15 kV. For an applied voltage of 10 kV, the injection was retarded for a period until the electrostatic force was strong enough to inject the solution jet, and some of the nanofibers were fused together as a bundle of fibers. If the applied electrical voltage was greater than 20 kV, the extraction rate of the polymer solution was too fast to evaporate the solvent. Thus, wet nanofibers were fused together to form a bundle morphology.

Another type of PAN carbon nanofiber with a nanometer porous structure in individual electrospun nanofibers can be produced by blending a sacrificial polymer (e.g., PMMA) into a PAN solution [23]. After thermal treatment, the decomposition of the PMMA results in the formation of a porous structure. The use of PAN-based blends is recognized as an efficient way to create a hierarchical porous structure in carbon nanofibers. Gbewonyo et al. [23] observed that the introduction of PMMA and silica nanoparticles to PAN polymer solutions enabled the fabrication of a carbon nanofibrous mat with a unique hierarchical porous structure via the electrospinning process. However, it reduced thermal conductivity by 98% compared to the non-porous carbon film. Zhou et al. [24] proposed a new method to adopt a metal-free reversible addition–fragmentation chain-transfer polymerization of poly(acrylonitrile-block-methyl methacrylate), followed by electrospinning, stabilization, and carbonization. This new method produced porous nanofibers with a specific surface area of 503 m^2/g, higher than those samples formed by traditional methods.

Porosity development in relation to a high specific surface area and micropore volume is very important for carbon nanofibers, depending on their application. Different structures (such as core/shell, hollow, and porous) of carbon nanofibers have been produced using electrospinning techniques, which have become a straightforward and convenient way to produce continuous and porous carbon nanofibers [12]. These porous nanofibers have great potential for use in drug delivery and as a scaffold for tissue engineering [25], in the capacitive deionization process for water treatment [26], or in energy [27–30]. However, there is very little application in gas adsorption. To reduce the impacts of global warming, the capture of carbon dioxide (CO_2) is important. Moreover, the ultramicropore volume, specific surface area, and nitrogen-containing functional groups of adsorbents are regarded as the major features affecting the CO_2 adsorption capacities of the adsorbents. Therefore, the aim of this study was to synthesize polyacrylonitrile (PAN)-based activated carbon nanofibers (ACNFs) using electrospinning processes for the capture of CO_2. Using a sacrificing core or pore generator, i.e., poly(methyl methacrylate) (PMMA), solid, hollow, or porous ACNFs were prepared. Through electrospinning, followed by stabilization, carbonization, and activation, ACNFs were formed with different porous structures. Several properties of the ACNFs with different porous structures were characterized, and the CO_2 adsorption on the ACNFs was investigated.

2. Materials and Methods

2.1. Preparation of Electrospun Nanofibers

Polyacrylonitrile (PAN)-based carbon nanofibers with different porous structures were prepared using electrospinning processes, including solid, hollow, and porous nanofibers. The hollow nanofibers were synthesized using a coaxial electrospinning process in which PAN (Mw = 150 kDa, Sigma–Aldrich, St. Louis, MO, USA) was the shell polymer and poly(methyl methacrylate) (PMMA) (Mw = 120 kDa, Sigma–Aldrich) was selected as the sacrifice core. Initially, PAN and PMMA were dissolved in N, N-dimethylacetamide (DMAc, Sigma–Aldrich) individually to form the polymer solutions with 10 wt.% PAN or 30 wt.% PMMA. The resulting solutions were subjected to magnetic stirring at 60 °C for 24 h in order to obtain homogeneous polymer solutions. The core–shell fibers were prepared using a coaxial spinneret system in an electrospinning unit (FES-COE, Falco Tech Enterprise Co., Ltd., New Taipei City, Taiwan). The inner diameter of the outer needle (18 gauge) was 0.96 mm, and the inner and outer diameters of the inner needle (21 gauge) were 0.52 and 0.82 mm, respectively. The electrospinning was carried out under an applied electrical voltage of 15 kV onto a metal drum collector (∅ 10 cm) covered with aluminum foil and rotated at 300 rpm, and a tip-to-collector distance of 20 cm was used. The shell and core solutions were pumped at a flow rate of 1.0 and 0.5 mL/h [22], respectively, and pushed by two syringe pumps (NE-1000, New Era Pump Systems, Inc., Farmingdale, NY, USA).

The core–shell fiber was stabilized in air from room temperature to 280 °C at a heating rate of 1 °C/min, then the temperature was held at 280 °C for 12 h to complete the cyclization and dehydrogenation reactions before the carbonization process to convert PAN from thermoplastic to a non-plastic compound [28,31,32]. The stabilized nanofibers were cooled down to room temperature and then carbonized in a nitrogen atmosphere with a flow of 100 sccm in a tubular furnace at 900 °C with a heating rate of 5° C/min, and maintained for 1 h [28] before the sample was cooled down to room temperature. After carbonization, activation of the samples was carried out by raising the temperature to 850 °C at a rate of 10° C/min under flowing nitrogen. CO_2 was used as the activation agent with a flow rate of 100 sccm, switched in and held for 1 h. This sample was labeled as PANh15. For comparison, the PMMA (core polymer) was replaced with PAN, and the other conditions remained the same. This solid sample was the control sample and was denoted as PANf. Another type of core–shell fiber was synthesized under an applied electrical voltage of 12 kV, and the shell and core solutions were pumped at a flow rate of 0.7 and 0.3 mL/h, respectively. The other treatments remained the same, and this sample was denoted as PANh12.

In addition, the porous fibers were obtained from a copolymer that was electrospun using a traditional single spinneret system, where PMMA was selected as the pore generator. First, a mixture of PAN and PMMA was dissolved in DMAc by stirring for 24 h at 60 °C to obtain a blend solution for electrospinning. The blend ratio of PAN and PMMA was 2:1 (w/w), and the total polymer concentration was 15 wt.%. The blend solution was loaded into a syringe with a 21-gauge spinneret (0.52 mm inner diameter). The infusion rate of the solution in the syringe was 1.0 mL/h. The applied voltage was 15 kV, and a tip-to-collector distance of 15 cm was chosen. The follow-up processes remained the same, and this sample was labeled as PANp.

2.2. Characterizations

The morphology of the samples was observed using field emission scanning electron microscopy (FESEM) with a microscope (S-4700, Hitachi, Krefeld, Germany). The surface feature of the samples was deduced from N_2 adsorption–desorption isotherms measured at –196 °C using an ASAP 2020 accelerated surface area and porosimetry system (Micromeritics, Norcross, GA, USA). Prior to the adsorption measurements, all samples were degassed at 350 °C for 24 h. The specific surface areas (SSAs) of the samples were measured in P/P_o = 0.05 ~ 0.3 using the Brunauer–Emmett–Teller (BET) method. The micropore (<2.0 nm)

surface area (S_{mi}) was determined using the t-plot method. The single point total pore volume (V_t) was obtained at $P/P_o \approx 0.99$. The mesopore volume (V_{me}), micropore volume (V_{mi}), and ultramicropore (<0.7 nm) volume ($V_{<0.7\,nm}$) were calculated by applying a non-local density functional theory (NLDFT) model, where $V_{<0.7\,nm}$ is part of V_{mi}. The pore size distribution curves were also obtained from a NLDFT model. X-ray photoelectron spectroscopy (XPS) was utilized to determine the number and type of functional groups present on the surface of the samples. The XPS spectra of all samples were collected using a spectrophotometer (PHI 5000 VersaProbe II, ULVAC-PHI, Kanagawa, Japan), in which a scanning X-ray monochromator (Al Anode, hν = 1401 eV) was used and the information on the elements within a few nanometers of the sample surface could be obtained. For calibration purposes, the C 1s electron binding energy (B.E.) that corresponds to graphitic carbon was set at 284.6 eV. A nonlinear least squares curve-fitting program (XPSPEAK software, version 4.1, The Chinese University of Hong Kong, Hong Kong, China) was used for the deconvolution of the XPS spectra.

2.3. CO_2 Adsorption Isotherms

The CO_2 adsorption isotherms on all the samples were measured using the Micromeritics ASAP 2020 system. Prior to measurement, a sample of approximately 0.05 g was outgassed at 350 °C for 24 h to remove the adsorbed contaminants. The equilibration interval for each pressure point was 45 s, and the CO_2 pressure ranged from 0 to 123 kPa. The temperature during the CO_2 adsorption process was maintained at 25, 40, or 55 °C using a circulating water bath thermostat. The interaction between the adsorbate molecules and the adsorbent lattice atoms can be predicted by the isosteric heat of adsorption (Q_{st}), which can be used as a measure of the energetic heterogeneity of a solid surface [33]. The Q_{st} can be estimated using the Clausius–Clapeyron equation, shown in Equation (1):

$$-\frac{Q_{st}}{R} = \left(\frac{d\ln P}{d\,\frac{1}{T}}\right), \quad (1)$$

where Q_{st} (kJ/mol) is the isosteric heat of adsorption, R (=8.314 J/mol/K) is the gas constant, P (kPa) is the CO_2 pressure, and T (K) is the adsorption temperature. A Pearson correlation analysis was performed to explore the relationships between the CO_2 adsorption capacity and the surface features, and the nitrogen-containing functional groups of the adsorbents.

2.4. CO_2 Adsorption Column Experiments

A fixed-bed reactor was utilized to carry out the adsorption column breakthrough curves of CO_2 on all samples according to the ASTM D5160-95 method [34] at 25, 40, or 55 °C. A sample of 0.4–0.7 g was loaded into a glass tube with an inner diameter of 1 cm and a length of 20 cm, with a packed height of 10 cm. The glass tube was covered with a stainless steel sleeve on which a heating strip was wound to control the temperature of the fixed bed, and a thermocouple was positioned on the surface of the glass tube to monitor the temperature of the adsorption bed. Typical untreated flue gas compositions from a power plant burning low sulfur coal contain approximately 15–16% of CO_2 [35,36]. Thus, the CO_2 concentration was set at 15%, and was supplied by CO_2 and N_2 cylinders under appropriate mixing and quantified by gas chromatography with a thermal conductivity detector (GC/TCD). The total flow rate of the gas stream was 20 sccm. The CO_2 concentration at the exit was measured using GC/TCD. When the exit concentration reached the inlet concentration, the adsorbent was heated to 150 °C to cause CO_2 desorption and to regenerate the adsorbent in the nitrogen atmosphere. The Yoon and Nelson equation (Equation (2)) was used for data fitting, which is a semi-empirical gas adsorption model that could predict the whole breakthrough curve [37]:

$$\frac{C}{C_0} = \frac{1}{1 + exp[k'(\tau - t)]}, \quad (2)$$

where C is the outlet concentration at time t (mmol/cm^3), C_0 is the inlet concentration of CO_2 (mmol/cm^3), k' is the rate coefficient (1/min), τ is the time at 50% breakthrough (min), and t is the breakthrough time (min). Adsorption–desorption cyclic tests were performed to evaluate the regeneration of the adsorbents. A total of 10 successive breakthrough experiments were conducted.

3. Results and Discussion

3.1. FESEM Images

In order to ensure that carbonization at 900 °C for 1 h was an appropriate process to cause the thermal decomposition of PMMA, the FESEM images were observed for the carbonized samples, as shown in Figure 1. These images clearly demonstrate the formation of hollow tubular structures for PANh15 (Figure 1a) and PANh12 (Figure 1b). Figure 1c is the cross-section of PANp, which displays several pores that were well distributed in the nanofibers. Since the pores were small and dispersed, a high magnification was needed to clearly identify the pores. These images show that the PMMA in the core or in the fibers experienced a variety of intrinsic thermal degradation processes, such as depolymerization, random scission, and side-group elimination, and finally formed volatile degradation products [19].

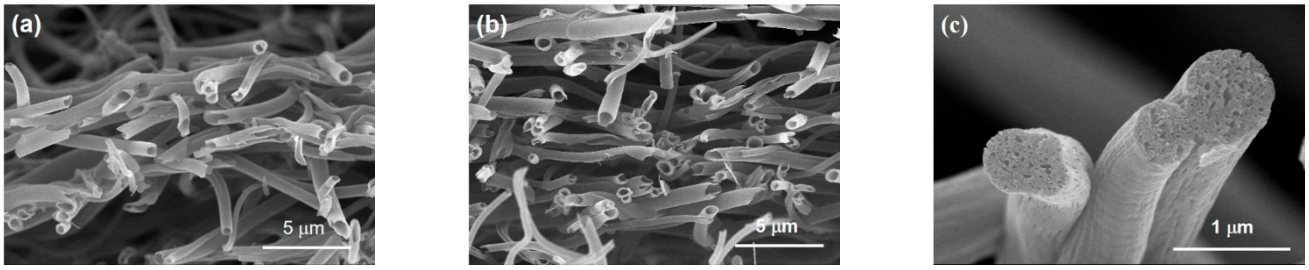

Figure 1. FESEM images of the carbonized samples of: (**a**) PANh15; (**b**) PANh12; (**c**) PANp.

The surface morphology of all samples is illustrated in Figure 2A–D and their cross-sections are shown in Figure 2a–d. The nanofibers were randomly distributed with uniform sizes and little directionality. PANf was prepared using coaxial electrospinning with the same core and shell solutions. However, the resultant nanofibers were merged without demarcations. Although the surface of nanofibers in a lower magnification was smooth, the surface of nanofibers was, in fact, uneven (Figure 2a–d), especially for PANp. This evidently indicates that the evaporation of volatile compounds from PMMA and PAN in the carbonization and activation stages generated pores on the wall or fibers. The diameters of PANf and PANp from Figure 2a,d were approximately 500 and 900 nm, and the outer diameters of PANh15 (Figure 2b) and PANh12 (Figure 2c) were approximately 800 and 870 nm with a shell thickness of 77 and 106 nm, respectively. The results imply that the volatile compounds from the thermal decomposition of PMMA were expected to escape from the longitudinal and lateral directions of the nanotubes. It is believed that the removal of PMMA retarded or hindered the fiber shrinkage such that the hollow fibers and PANp possessed larger fiber sizes. In addition, comparing PANh15 with PANh12, the larger applied voltage and injection rates of polymers produced smaller fiber sizes and shell thickness. Figure 2d indicates that PMMA and PAN in copolymer solution were uniformly distributed during the electrospinning process.

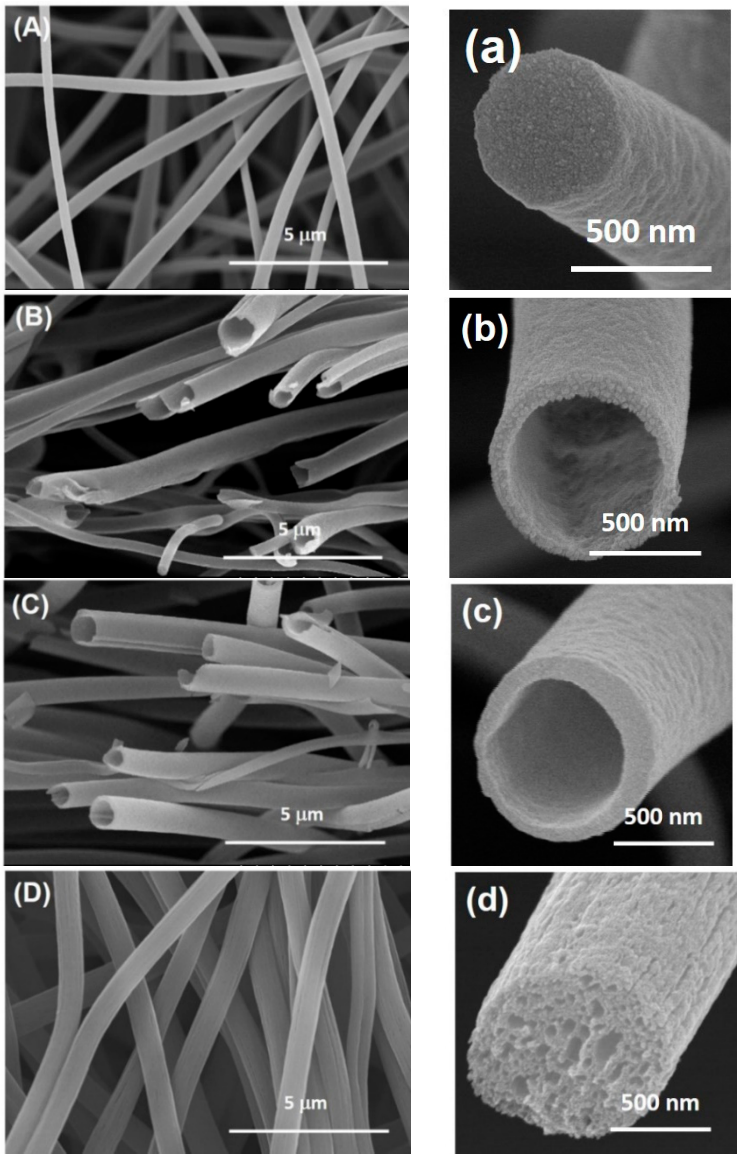

Figure 2. FESEM images of the ACNFs: (**A**,**a**) PANf; (**B**,**b**) PANh15; (**C**,**c**) PANh12; (**D**,**d**) PANp.

3.2. ASAP Data

Figure 3a shows the N_2 adsorption–desorption isotherms of all the samples at –196 °C. The adsorption isotherms for PANf, PANh15, and PANh12 were essentially type I according to the Brunauer–Emmett–Teller (BET) classification, and the desorption branch almost superimposed on the adsorption branch, which is indicative of microporosity. However, PANp exhibited a different pattern, in which the adsorption isotherm represented type IV features with a distinct hysteresis loop at a relative pressure between 0.42 and 1.0. This hysteresis loop was identified as H3 according to the International Union of Pure and Applied Chemistry (IUPAC) classification, indicating the existence of mesoporosity and microporosity. The pore size distributions in the 0.4–2 nm and 5–20 nm ranges are shown in Figure 3b,c, respectively, which were derived from the NLDFT model. The main micropores for all samples were at approximately 0.6 nm, and a peak occurring at 0.4–0.5 nm was also found on PANf and PANh15. Additionally, a large peak at around 0.6 nm was observed on PANh12. The above were classified as ultramicropores (pore size less than 0.7 nm). It is noted that PANp had significant pore volumes at 5–20 nm, in response to the hysteresis loop in the N_2 isotherms.

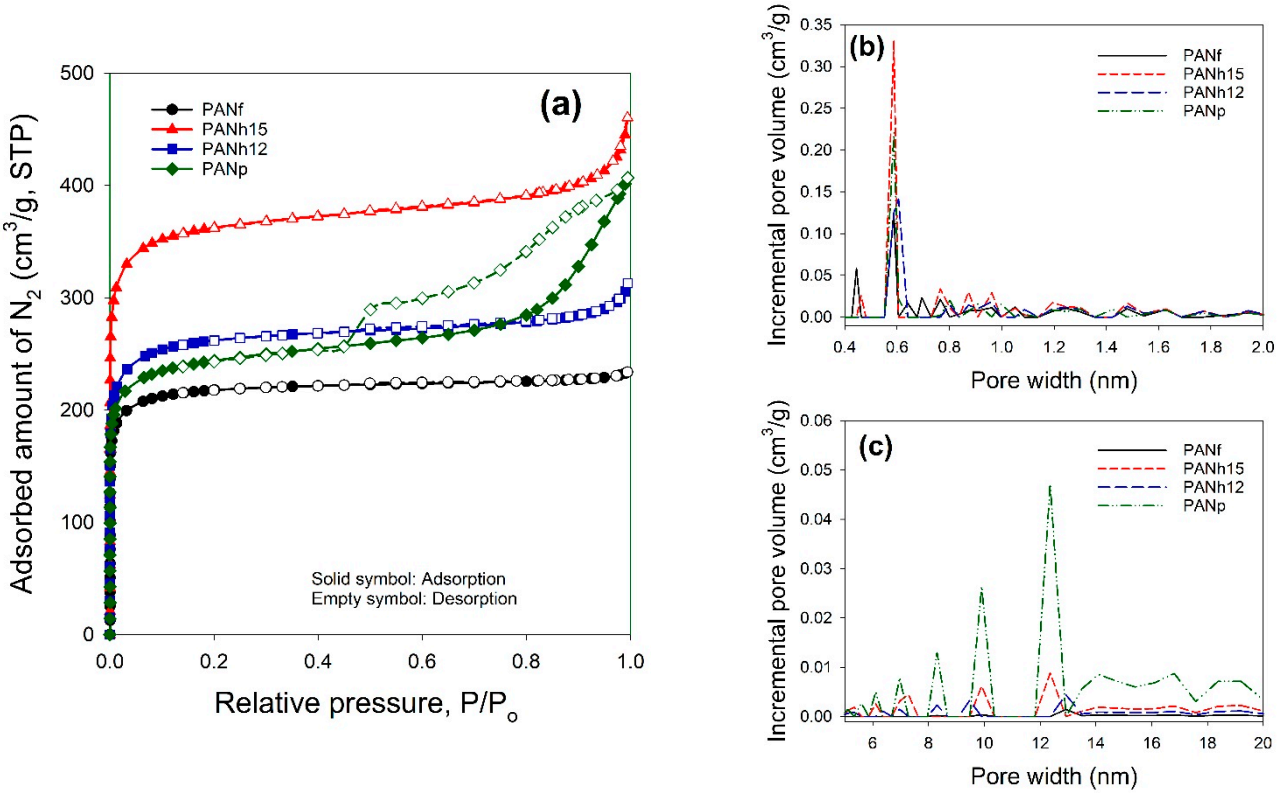

Figure 3. N_2 adsorption–desorption data at −196 °C for the ACNFs: (**a**) isotherms; (**b**) pore size distributions (0.4–2 nm); (**c**) pore size distributions (5–20 nm).

Table 1 summarizes the surface features of the samples determined from the N_2 adsorption–desorption isotherms. The BET specific surface areas (SSAs) of PANf, PANh15, PANh12, and PANp were 733, 1222, 884, and 825 m^2/g. The micropore and ultramicropore volumes both followed the order PANh15 > PANh12 > PANp > PANf, though the total pore volume of PANh12 was less than that of PANp. The ratios of surface areas and pore volumes obtained from the N_2 adsorption–desorption data at –196 °C for all samples are shown in Figure 4. PANp held a large amount of mesopore. Despite PANf having a smaller surface area and pore volume, its microporosity was conspicuous.

Table 1. Surface feature of the samples determined from N_2 adsorption–desorption isotherms.

Sample	SSA $^{\alpha}$ (m^2/g)	S_{mi} $^{\beta}$ (m^2/g)	V_t $^{\gamma}$ (cm^3/g)	V_{ma} $^{\varphi}$ (cm^3/g)	V_{me} $^{\eta}$ (cm^3/g)	V_{mi} $^{\eta}$ (cm^3/g)	$V_{<0.7\ nm}$ $^{\eta}$ (cm^3/g)	r_p $^{\xi}$ (nm)	q_{CO_2} $^{\Phi}$ (mmol/g) at 25 °C	
									0.15 atm	1 atm
PANf	733	617	0.3616	0.0125	0.0106	0.3385	0.2227	0.457	0.97	2.95
PANh15	1222	996	0.7121	0.0485	0.1038	0.5598	0.3558	0.476	0.86	3.04
PANh12	884	709	0.4840	0.0299	0.0490	0.4050	0.2665	0.503	0.94	3.16
PANp	825	624	0.6293	0.0256	0.2415	0.3622	0.2429	0.735	0.88	2.86

$^{\alpha}$ SSA (specific surface area) was determined using the BET method. $^{\beta}$ S_{mi} was determined using the t-plot method. $^{\gamma}$ V_t represented the single point total pore volume at $P/P_o \approx 0.99$. $^{\eta}$ V_{me}, V_{mi}, and $V_{<0.7\ nm}$ were determined using a non-local density functional theory (NLDFT) model. $^{\varphi}$ V_{ma} was obtained by subtraction. $^{\xi}$ r_p (average pore hydraulic radius) was determined using the micropore analysis (MP) method. $^{\Phi}$ q_{CO2} was the CO_2 amount adsorbed on the samples determined using the ASAP2020 at 0.15 and 1 atm (298 K).

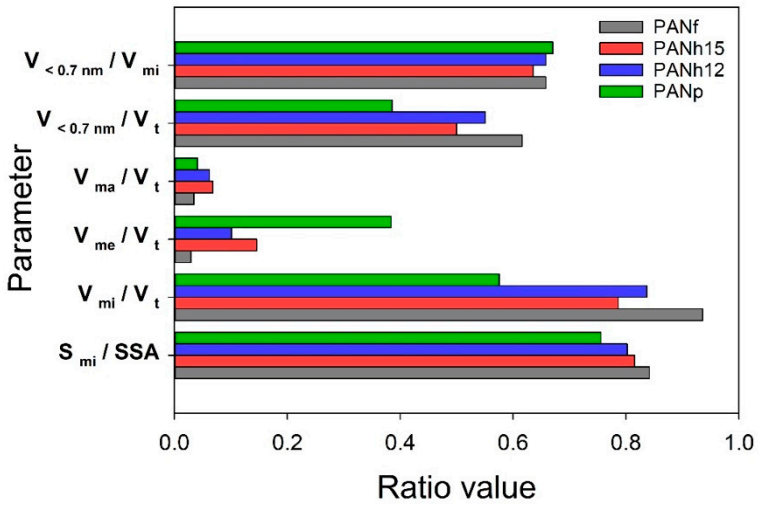

Figure 4. The ratios of surface areas and pore volumes obtained from N_2 adsorption–desorption data at −196 °C for all samples.

3.3. XPS Data

PAN is characterized with the C ≡ N group. In order to understand the change of nitrogen-containing functional groups undergoing subsequent electrospinning, stabilization, carbonization, and activation processes, XPS was conducted to explore the surface elemental compositions and their chemical states. The XPS survey scan spectra of the samples indicated that the major peaks were due to the C 1s, N 1s, and O 1s photoelectrons. Figure 5 shows the atomic ratios of C 1s, N 1s, and O 1s of the samples. The atomic ratio of N 1s followed the order PANp > PANf > PANh15 > PANh12, which indicated that a larger amount of nitrogen enabled the loss of the hollow nanofibers in the manufacture processes.

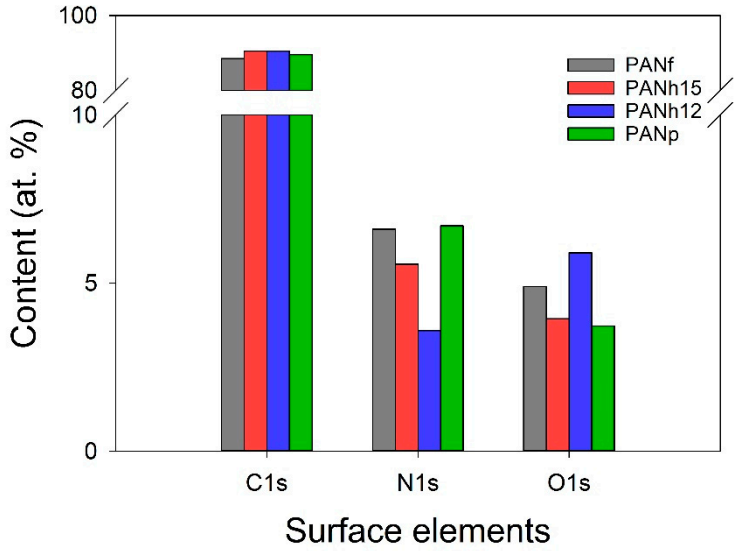

Figure 5. The atomic ratios of C 1s, N 1s, and O 1s obtained from the X-ray photoelectron spectroscopy (XPS) of the samples.

The curve-fitting for the high resolution XPS N 1s spectra [38–40] for all the samples is shown in Figure 6. The N 1s spectra were decomposed into, at most, seven identified components. Table 2 displays the percentages of nitrogen-containing functional groups. The peak at 395.7 eV was the aromatic N-imines; the peak at 398.4 eV represented the pyridine-type N; the peak at 400.1 eV was the pyrrole or pyridone; the peak at 401.2 eV showed the quarternary N; the peak at 402.4 eV indicated the pyridine-N oxides; and the

peak at 404 eV was the shake-up satellites. The contribution of chemisorbed NO_2 was assigned at 405 eV. PANf and PANh15 had a higher percentage of the pyrrole or pyridone (400.1 eV) and pyridine-type N (398.4 eV), while the pyridine-type N (398.4 eV) and the quarternary N (401.2 eV) were predominant on PANh12 and PANp. In summary, PANh15 had the highest percentage of pyrrole or pyridone of the five-member or six-member rings, and the pyridine-type N groups of the six-member rings were the primary functional groups on the others. In addition, PANh12 showed a higher percentage of the quarternary N and pyridine-N oxides in comparison with the others.

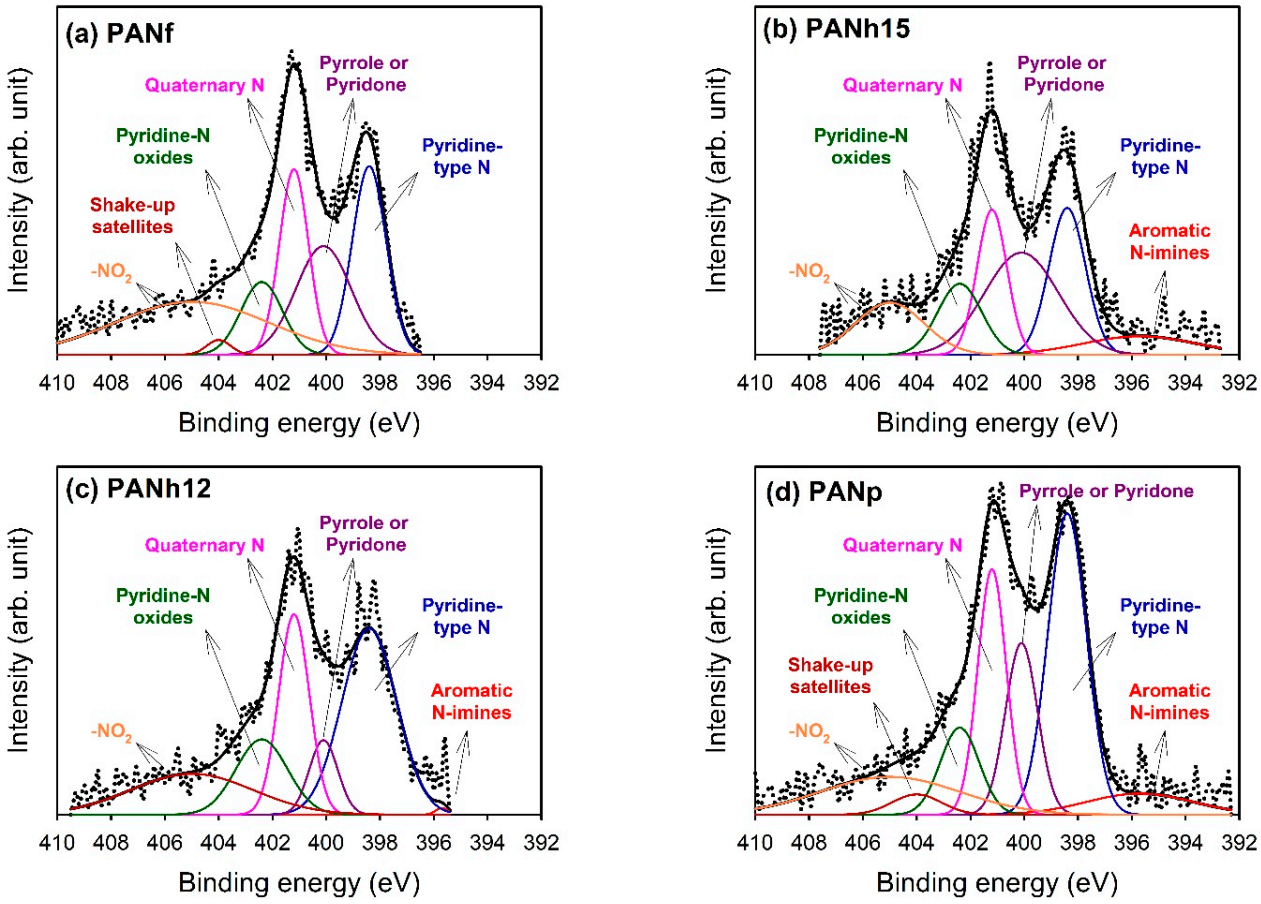

Figure 6. Results of the fits of the high resolution X-ray photoelectron spectroscopy (XPS) N 1s region: (**a**) PANf; (**b**) PANh15; (**c**) PANh12; (**d**) PANp. The values were given in atomic ratio (%) of total intensity.

Table 2. Results of the fits of the XPS N_{1s} region, values shown at. % of total intensity.

Sample	Binding Energy (eV)						
	395.7	398.4	400.1	401.2	402.4	404	405
	Aromatic N-imines	Pyridine -Type N	Pyrrole or Pyridone	Quarternary N	Pyridine-N oxides	Shake-Up Satellites	NO_2
PANf	—	21.8	20.5	18.4	10.3	1.2	27.8
PANh15	8.0	20.6	29.1	16.7	11.9	—	13.7
PANh12	0.3	37.2	7.7	22.4	14.2	—	18.2
PANp	6.2	32.2	15.3	19.5	9.4	2.8	14.7

3.4. CO_2 Adsorption Equilibrium

The adsorption equilibrium isotherms of CO_2 on all samples at different temperatures (25, 40, and 55 °C) are shown in Figure 7. With increasing pressure and a decreasing temperature, the CO_2 adsorbed amounts increased. This demonstrated that CO_2 adsorption at 25 to 55 °C on the samples was exothermic. At 25 °C and 1 atm, the adsorption amounts of CO_2 on PANf, PANh15, PANh12, and PANp were 2.95, 3.04, 3.16, and 2.86 mmol/g, respectively, which were superior to that of commercial activated carbon fibers with a fiber size of approximately 6.8 μm (1.92 mmol/g) [41]. The CO_2 uptake at 25 °C and 0.15 atm (a typical untreated flue gas composition) followed the order PANf (0.97 mmol/g) > PANh12 (0.94 mmol/g) > PANp (0.88 mmol/g) > PANh15 (0.86 mmol/g). These data are also shown in Table 1. Table 3 summarizes the CO_2 adsorption amounts in this work with various related adsorbents in the literature. Compared with our previous studies, the carbonization temperature in this work was higher in order to completely remove the PMMA. It is believed that the carbonization temperature was too high to get a high CO_2 uptake.

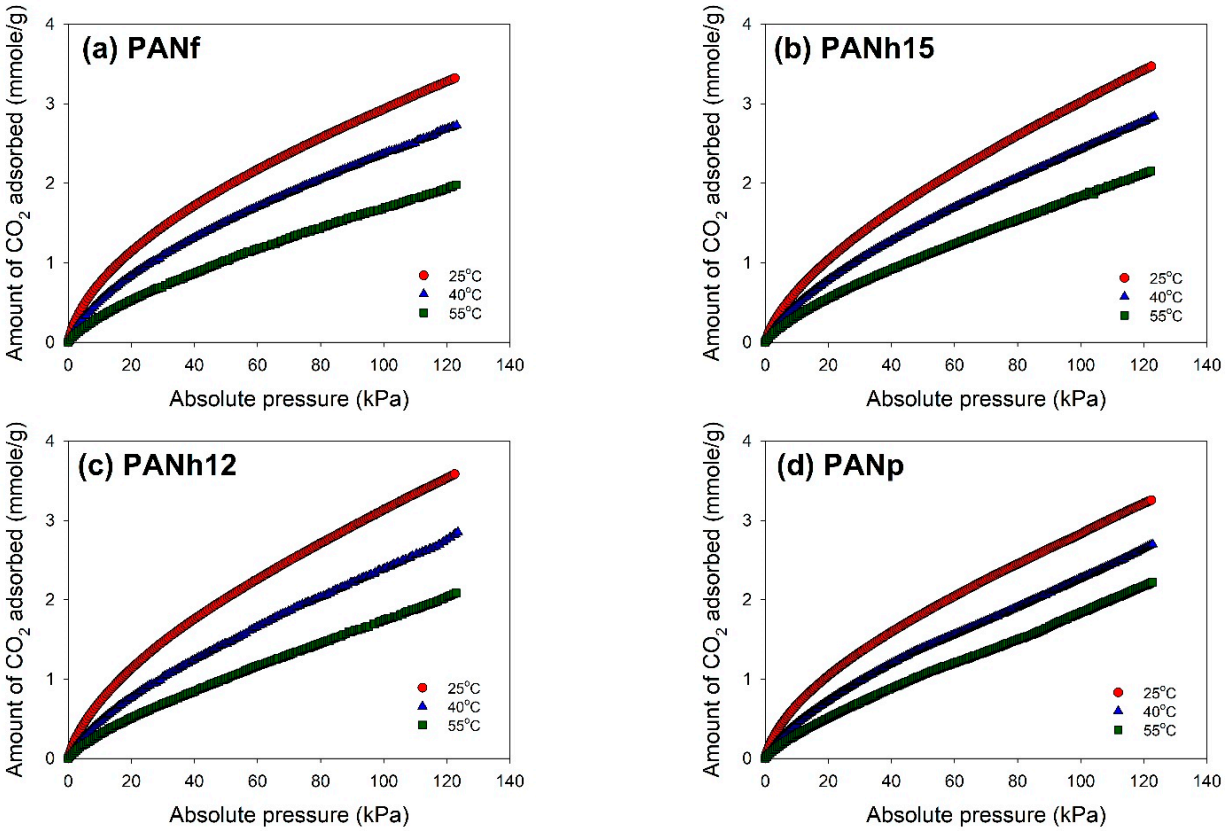

Figure 7. Adsorption isotherms of CO_2 of the ACNFs: (**a**) PANf; (**b**) PANh15; (**c**) PANh12; (**d**) PANp.

The Q_{st} values changing with the CO_2 loading (0.2 to 1.2 mmol/g) are shown in Figure 8, where the Q_{st} values log-linearly decreased with the CO_2 loading. This phenomenon implies that the active sites on the surface of ACNFs were energetically heterogeneous for CO_2 adsorption [42]. In addition, the enhanced micropore confinement or the interactions between CO_2 molecules and the nitrogen-containing functional groups [43] could be responsible for the higher Q_{st} values at a lower CO_2 loading. According to the Q_{st} values, almost lower than 40 kJ/mole, it was indicative of a typical physical adsorption for the CO_2 adsorption on these adsorbents.

In addition, in investigating the important properties of adsorbents for the CO_2 adsorption capacity, it was observed that the CO_2 uptake at 0.15 atm had high correlation coefficients with chemisorbed NO_2 and the ratio of $V_{<0.7\,nm}$ to V_t using the Pearson

correlation analysis. Moreover, the CO_2 uptake at 1 atm was highly related to pyridine-N oxides and the ratio of V_{mi} to V_t.

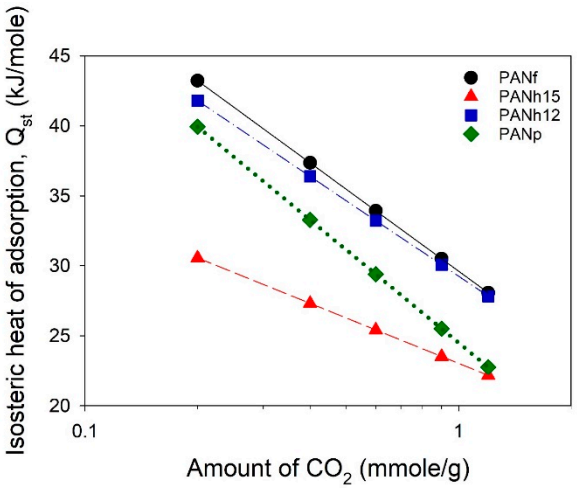

Figure 8. The isosteric heat of adsorption of CO_2 on the samples.

Table 3. Comparisons of CO_2 uptakes on the adsorbents in this study with various support materials using electrospinning in the literature.

Adsorbent	Precursor	SSA (m^2/g)	Conc. of CO_2	Temp. (°C)	CO_2 Uptake (mmol/g)	Reference
Hollow ACNFs [α]	PAN	884	1 atm 0.15 atm	25	3.16 0.94	This study
ACNFs	PAN	872	1 atm 0.15 atm	25	3.47 1.01	[44]
CNFs [β]	PAN	306	1 atm 0.15 atm	25	2.52 1.11	[44]
ACNFs	PAN	486	1 bar 0.15 bar	25	2.25 1.09	[45]
CNFs	PAN	12	1 bar	25	0.55	[46]
ACNFs	PAN, polyvinylidene fluoride	925	1 bar	25	2.21	[46]
ACNFs	PAN	412	1 bar	25	0.92	[47]
ACNFs	PAN Melamine	547	1 bar	25	1.44	[47]
CNFs	PAN	966	1 bar	25	2.9	[48]
ACNFs	PAN	897	1 atm 0.15 atm	25	3.17 1.00	[49]
ACFs [γ]	PAN	966	1 atm	25	2.33	[41]

[α] ACNFs: activated carbon nanofibers; [β] CNFs: carbon nanofibers; [γ] ACFs: activated carbon fibers.

3.5. CO_2 Adsorption Breakthrough Curves

Figure 9 shows the adsorption breakthrough curves of CO_2 at different temperatures on the samples. The CO_2 concentration was 15%. The Yoon and Nelson equation (Equation (2)) was adopted for breakthrough data fitting, which could predict the whole breakthrough curve. The fitting results are listed in Table 4 and also plotted in Figure 9. The values of R-squared suggest that the Yoon and Nelson equation fitted the data well in the whole range. The adsorption breakthrough wave was not sharp for PANf (at 25 °C) and PANh15 (at 25 and 40 °C), which could account for the larger pore diffusion resistance [50] due to smaller nanofiber sizes or a large micropore volume. This feature was in relation to the values of the rate coefficient, k'. The rate coefficients in this work did not exhibit large variations. Moreover, the highest rate coefficient took place on the curves at 40 °C except

for PANh15, which implies that the pore diffusion resistance was weak at 40 °C. In order to determine the regeneration of these samples, PANh15 was selected as an example to carry out the adsorption–desorption runs 10 times. Successive cyclic adsorption breakthrough curves and the variation of time at C/C_0 = 0.1 and 0.5 are shown in Figure 10. The data demonstrates that after 10 adsorption–desorption cyclic tests, this adsorbent maintained its CO_2 adsorption capacities without appreciable degradation.

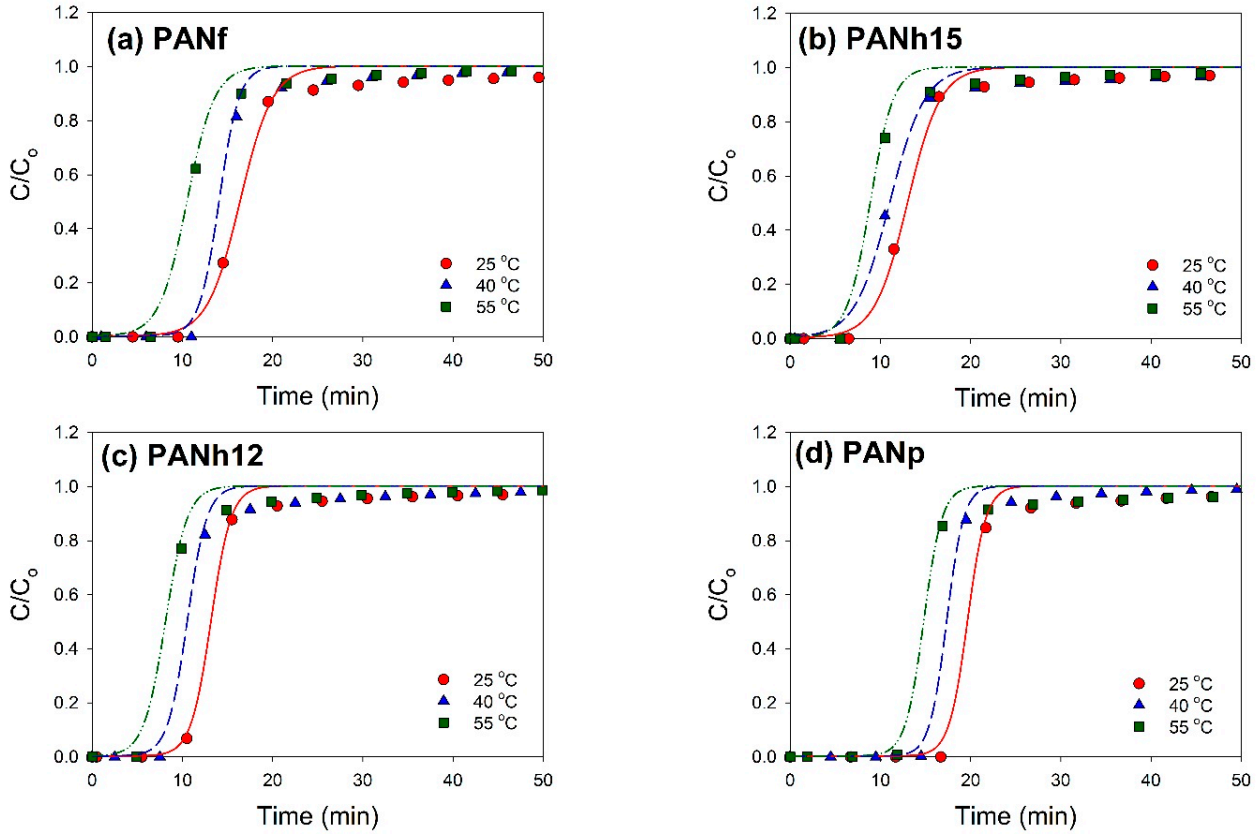

Figure 9. Adsorption breakthrough curves of CO_2 at different temperatures on the samples: (**a**) PANf; (**b**) PANh15; (**c**) PANh12; (**d**) PANp. The lines are the fitted results using the Yoon and Nelson equation.

Table 4. Fitted parameters of the Yoon and Nelson equation for the CO_2 adsorption breakthrough data on the samples at different temperatures.

Sample	Temp. (°C)	τ (min)	K′ (1/min)	R^2
PANf	25	16.40	0.553	0.99009
	40	14.07	0.904	0.99453
	55	10.52	0.655	0.99294
PANh15	25	13.01	0.547	0.99352
	40	11.04	0.515	0.99093
	55	8.87	0.779	0.99147
PANh12	25	13.17	0.895	0.99363
	40	10.54	0.918	0.99206
	55	8.14	0.827	0.98918
PANp	25	19.65	0.977	0.99107
	40	17.34	1.057	0.99462
	55	14.80	0.980	0.98692

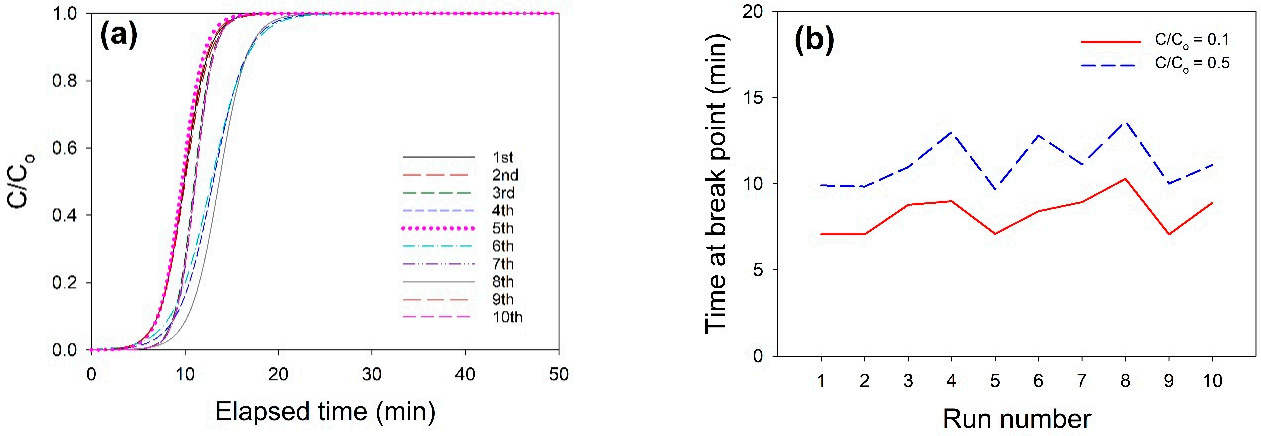

Figure 10. (**a**) Successive cyclic adsorption breakthrough curves, and (**b**) the variation of time at C/C_0 = 0.1 and 0.5.

4. Conclusions

This study successfully fabricated hollow ACNFs and porous ACNFs using the electrospinning technique. The ACNFs with different pore structures displayed distinctive features of N_2 isotherms. The carbonization at 900 °C was appropriate to completely decompose and remove the PMMA, but a high carbonization temperature decreases the CO_2 uptake, compared with previous studies. The solid ACNFs exhibited the highest microporosity, while the hollow ACNFs and porous ACNFs displayed higher specific surface areas than that of the solid ACNFs. The CO_2 adsorption of the ACNFs was an exothermic reaction, and the performance was highly related to the surface features and the nitrogen groups. The Yoon and Nelson equation could be adopted to fit well with the CO_2 adsorption breakthrough data. The cyclic tests demonstrated that the breakthrough points in the curves were almost unchanged after 10 adsorption–desorption runs, which indicates that the hollow ACNFs are promising adsorbents. These ACNFs exhibited a good CO_2 adsorption capacity and an excellent cyclic operation performance. These are the keys to CO_2 capture in industrial applications.

Author Contributions: Conceptualization, Y.-C.C.; methodology, Y.-C.C.; software, C.-C.H.; validation, Y.-C.C.; investigation, W.-T.C.; data curation, C.-C.H. and W.-T.C.; writing—original draft preparation, Y.-C.C.; writing—review and editing, Y.-C.C.; visualization, Y.-C.C.; supervision, Y.-C.C.; project administration, Y.-C.C.; funding acquisition, Y.-C.C. All authors have read and agreed to the published version of the manuscript.

Funding: This research was funded by the Ministry of Science and Technology, Taiwan, grant numbers MOST 107-2221-E-155-002- and MOST 108-2221-E-155-038-.

Institutional Review Board Statement: Not applicable.

Informed Consent Statement: Not applicable.

Data Availability Statement: The data presented in this study are available on request from the corresponding author. The data are not publicly available due to privacy restrictions.

Acknowledgments: The authors would like to thank the Instrumentation Center at NTU for performing the FESEM and EA analyses, the Department of Chemical Engineering at NTU for performing the N_2 adsorption–desorption analysis, and the Instrumentation Center at NTHU for performing the XPS analysis.

Conflicts of Interest: The authors declare no conflict of interest.

References

1. Huang, Z.M.; Zhang, Y.Z.; Kotaki, M.; Ramakrishna, S. A review on polymer nanofibers by electrospinning and their applications in nanocomposites. *Compos. Sci. Technol.* **2003**, *63*, 2223–2253. [CrossRef]

2. Nasouri, K.; Shoushtari, A.M.; Kaflou, A. Investigation of polyacrylonitrile electrospun nanofibres morphology as a function of polymer concentration, viscosity and Berry number. *Micro Nano Lett.* **2012**, *7*, 423–426. [CrossRef]
3. Ondarçuhu, T.; Joachim, C. Drawing a single nanofiber over hundreds of microns. *Eur. Phys. Lett.* **1998**, *42*, 215–220. [CrossRef]
4. Yang, X.; Liu, Y.; Li, J.; Zhang, X. Influence of thermal decomposition on morphologies and magnetic properties of iron nanofibres via electrospinning. *Micro Nano Lett.* **2011**, *6*, 967–970. [CrossRef]
5. Xing, X.; Wang, Y.; Li, B. Nanofiber drawing and nanodevice assembly in poly(trimethylene terephthalate). *Opt. Express* **2008**, *16*, 10815–10822. [CrossRef]
6. Feng, L.; Li, S.H.; Li, H.J.; Zhai, J.; Song, Y.; Jiang, L.; Zhu, D. Super hydrophobic surface of aligned polyacrylonitrile nanoflbers. *Angew. Chem. Int. Edit.* **2002**, *41*, 1221–1223. [CrossRef]
7. Martín, J.; Maiz, J.; Sacristan, J.; Mijangos, C. Tailored polymer-based nanorods and nanotubes by "template synthesis": From preparation to applications. *Polymer* **2012**, *53*, 1149–1166. [CrossRef]
8. Ma, P.X.; Zhang, R. Synthetic nano-scale fibrous extracellular matrix. *J. Biomed. Mater. Res.* **1999**, *46*, 60–72. [CrossRef]
9. Liu, G.; Ding, J.; Qiao, L.; Guo, A.; Dymov, B.P.; Gleeson, J.T.; Hashimoto, T.; Saijo, K. Polystyrene-block-poly(2-cinnamoylethyl methacrylate) nanofibers preparation, characterization, and liquid crystalline properties. *Chem. Eur. J.* **1999**, *5*, 2740–2749. [CrossRef]
10. Wang, J.; Ouyang, Z.; Ren, Z.; Li, J.; Zhang, P.; Wei, G.; Su, Z. Self-assembled peptide nanofibers on graphene oxide as a novel nanohybrid for biomimetic mineralization of hydroxyapatite. *Carbon* **2015**, *89*, 20–30. [CrossRef]
11. Doshi, J.; Reneker, D.H. Electrospinning process and applications of electrospun fibers. *J. Electrostat.* **1995**, *35*, 151–160. [CrossRef]
12. Zhang, L.; Aboagye, A.; Kelkar, A.; Lai, C.; Fong, H. A review: Carbon nanofibers from electrospun polyacrylonitrile and their applications. *J. Mater. Sci.* **2014**, *49*, 463–480. [CrossRef]
13. Greiner, A.; Wendorff, J.H. Electrospinning: A fascinating method for the preparation of ultrathin fibers. *Angew. Chem. Int. Ed.* **2007**, *46*, 5670–5703. [CrossRef]
14. Ahmadian, A.; Shafiee, A.; Aliahmad, N.; Agarwal, M. Overview of nano-fiber mats fabrication via electrospinning and morphology analysis. *Textiles* **2021**, *1*, 206–226. [CrossRef]
15. Koski, A.; Yim, K.; Shivkumar, S. Effect of molecular weight on fibrous PVA produced by electrospinning. *Mater. Lett.* **2004**, *58*, 493–497. [CrossRef]
16. Gupta, P.; Elkins, C.; Long, T.E.; Wilkes, G.L. Electrospinning of linear homopolymers of poly(methyl methacrylate): Exploring relationships between fiber formation, viscosity, molecular weight and concentration in a good solvent. *Polymer* **2005**, *46*, 4799–4810. [CrossRef]
17. Shenoy, S.L.; Bates, W.D.; Frisch, H.L.; Wnek, G.E. Role of chain entanglements on fiber formation during electrospinning of polymer solutions: Good solvent, non-specific polymer–polymer interaction limit. *Polymer* **2005**, *46*, 3372–3384. [CrossRef]
18. Hsu, C.M.; Shivkumar, S. Nano-sized beads and porous fiber constructs of poly(1′-caprolactone) produced by electrospinning. *J. Mater. Sci.* **2004**, *39*, 3003–3013. [CrossRef]
19. Zussman, E.; Yarin, A.L.; Bazilevsky, A.V.; Avrahami, R.; Feldman, M. Electrospun polyacrylonitrile/poly(methyl methacrylate)-derived turbostratic carbon micro-/nanotubes. *Adv. Mater.* **2006**, *18*, 348–353. [CrossRef]
20. Xie, W.; Khan, S.; Rojas, O.J.; Parsons, G.N. Control of micro- and mesopores in carbon nanofibers and hollow carbon nanofibers derived from cellulose diacetate via vapor phase infiltration of diethyl zinc. *ACS Sustain. Chem. Eng.* **2018**, *6*, 13844–13853. [CrossRef]
21. Zhang, L.; Hsieh, Y.L. Carbon nanofibers with nanoporosity and hollow channels from binary polyacrylonitrile systems. *Eur. Polym. J.* **2009**, *45*, 47–56. [CrossRef]
22. Kaerkitcha, N.; Chuangchote, S.; Sagawa, T. Control of physical properties of carbon nanofibers obtained from coaxial electrospinning of PMMA and PAN with adjustable inner/outer nozzle-ends. *Nanoscale Res. Lett.* **2016**, *11*, 186. [CrossRef]
23. Gbewonyo, S.; Carpenter, A.W.; Gause, C.B.; Mucha, N.R.; Zhang, L. Low thermal conductivity carbon fibrous composite nanomaterial enabled by multi-scale porous structure. *Mater. Des.* **2017**, *134*, 218–225. [CrossRef]
24. Zhou, Z.; Liu, T.; Khan, A.U.; Liu, G. Block copolymer–based porous carbon fibers. *Sci. Adv.* **2019**, *55*, 6852. [CrossRef]
25. Qu, H.; Wei, S.; Guo, Z. Coaxial electrospun nanostructures and their applications. *J. Mater. Chem. A* **2013**, *1*, 11513–11528. [CrossRef]
26. El-Deen, A.G.; Barakat, N.A.M.; Khalild, K.A.; Kim, H.Y. Hollow carbon nanofibers as an effective electrode for brackish water desalination using the capacitive deionization process. *New J. Chem.* **2014**, *38*, 198–205. [CrossRef]
27. Park, S.H.; Jung, H.R.; Lee, W.J. Hollow activated carbon nanofibers prepared by electrospinning as counter electrodes for dye-sensitized solar cells. *Electrochim. Acta* **2013**, *102*, 423–428. [CrossRef]
28. Wu, Y.; Gao, M.; Li, X.; Liu, Y.; Pan, H. Preparation of mesohollow and microporous carbon nanofiber and its application in cathode material for lithium–sulfur batteries. *J. Alloy. Compd.* **2014**, *608*, 220–228. [CrossRef]
29. Peng, Y.T.; Lo, C.T. Electrospun porous carbon nanofibers as lithium ion battery anodes. *J. Solid State Electrochem.* **2015**, *19*, 3401–3410. [CrossRef]
30. Zhang, T.; Qu, H.; Sun, K. Development of polydopamine coated electrospun PAN/PMMA nanofibrous membrane as composite separator for Lithium-ion batteries. *Mater. Lett.* **2019**, *245*, 10–13. [CrossRef]
31. Zhao, W.; Yamamoto, Y.; Tagawa, S. Regulation of the thermal reactions of polyacrylonitrile by c-irradiation. *Chem. Mater.* **1999**, *11*, 1030–1034. [CrossRef]

32. Qin, X.H. Structure and property of electrospinning PAN nanofibers by different preoxidation temperature. *J. Therm. Anal. Calorim.* **2010**, *99*, 571–575. [CrossRef]
33. Lee, J.S.; Kim, J.H.; Kim, J.T.; Suh, J.K.; Lee, J.M.; Lee, C.H. Adsorption equilibria of CO_2 on zeolite 13X and zeolite X/activated carbon composite. *J. Chem. Eng. Data* **2002**, *47*, 1237–1242. [CrossRef]
34. ASTM D5160-95. *Standard Guide for Gas.-Phase Adsorption Testing of Activated Carbon*; ASTM International: West Conshohocken, PA, USA, 2019.
35. Granite, E.J.; Pennline, H.W. Photochemical removal of mercury from flue gas. *Ind. Eng. Chem. Res.* **2002**, *41*, 5470–5476. [CrossRef]
36. Chou, C.T.; Chen, C.Y. Carbon dioxide recovery by vacuum swing adsorption. *Sep. Purif. Technol.* **2004**, *39*, 51–65. [CrossRef]
37. Huang, Z.H.; Kang, F.; Liang, K.M.; Hao, J. Breakthrough of methyethylketone and benzene vapors in activated carbon fiber beds. *J. Hazard. Mater. B* **2003**, *98*, 107–115. [CrossRef]
38. Biniak, S.; Szymanski, G.; Siedlewski, J.; Swiatkowski, A. The characterization of activated carbons with oxygen and nitrogen surface groups. *Carbon* **1997**, *35*, 1799–1810. [CrossRef]
39. Pamula, E.; Rouxhet, P.G. Bulk and surface chemical functionalities of Type III PAN-based carbon fibers. *Carbon* **2003**, *41*, 1905–1915. [CrossRef]
40. Raymundo-Pinero, E.; Cazorla-Amoros, D.; Linares-Solano, A. The role of different nitrogen functional groups on the removal of SO_2 from flue gases by N-doped activated carbon powders and fibers. *Carbon* **2003**, *41*, 1925–1932. [CrossRef]
41. Chiang, Y.C.; Hsu, W.L.; Lin, S.Y.; Juang, R.S. Enhanced CO_2 adsorption on activated carbon fibers grafted with nitrogen-doped carbon nanotubes. *Materials* **2017**, *10*, 511. [CrossRef]
42. Toth, J. Isotherm equations for monolayer adsorption of gases on heterogeneous solid surfaces. In *Fundamentals of Adsorption*; Myers, A., Belfort, G., Eds.; Engineering Foundation: New York, NY, USA, 1984; pp. 657–665.
43. To, J.W.F.; He, J.; Mei, J.; Haghpanah, R.; Chen, Z.; Kurosawa, T. Hierarchical N-doped carbon as CO_2 adsorbent with high CO_2 selectivity from rationally designed polypyrrole precursor. *J. Am. Chem. Soc.* **2016**, *38*, 1001–1009. [CrossRef]
44. Chiang, Y.C.; Lee, S.T.; Leo, Y.J.; Tseng, T.L. Importance of pore structure and surface chemistry in carbon dioxide adsorption on electrospun carbon nanofiber. *Sens. Mater.* **2020**, *32*, 2277–2288.
45. Xiong, L.; Wang, X.F.; Li, L.; Jin, L.; Zhang, Y.G.; Song, S.L.; Liu, R.P. Nitrogen-enriched porous carbon fiber as CO2 adsorbent with superior CO2 selectivity by air activation. *Energy Fuels* **2019**, *33*, 12558–12567. [CrossRef]
46. Heo, Y.J.; Zhang, Y.; Rhee, K.Y.; Park, S.J. Synthesis of PAN/PVDF nanofiber composites-based carbon adsorbents for CO_2 capture. *Composites B* **2019**, *156*, 95–99. [CrossRef]
47. Jeong, D.; Jie, W.; Adelodun, A.A.; Kim, S.; Jo, Y. Electrospun melamine-blended activated carbon nanofibers for enhanced control of indoor CO_2. *J. Appl. Polym. Sci.* **2019**, *136*, 47747. [CrossRef]
48. Ojeda-López, R.; Esparza-Schulz, J.M.; Pérez-Hermosillo, I.J.; Hernández-Gordillo, A.; Domínguez-Ortiz, A. Improve in CO_2 and CH_4 adsorption capacity on carbon microfibers synthesized by electrospinning of PAN. *Fibers* **2019**, *7*, 81. [CrossRef]
49. Chiang, Y.C.; Wu, C.Y.; Chen, Y.J. Effects of activation on the properties of electrospun carbon nanofibers and their adsorption performance for carbon dioxide. *Sep. Purif. Technol.* **2020**, *233*, 116040. [CrossRef]
50. Brasquet, C.; Cloirec, P.L. Adsorption onto activated carbon fibers: Applications to water and air treatments. *Carbon* **1997**, *35*, 1307–1313. [CrossRef]